Design and Stiffness Analysis of a XYZ Scanning Stage*

Kunhai Cai, Yanling Tian*, Liangyu Cui, Zhen Yang, Dawei Zhang
Key Laboratory of Mechanism Theory and Equipment Design of Ministry of Education
Tianjin University
Tianjin 300072, China
ckh881021@tju.edu.cn, meytian@tju.edu.cn

***Abstract*—A compact XYZ precision scanning stage is designed in this paper, which is assembled by a XY and a Z precision positioning stages. Each stage is driven by piezoelectric actuator, and guided by symmetric parallel flexible hinges, respectively. These parallel flexible hinges are arranged symmetrically to reduce cross-coupling among X-, Y- and Z-axis. In addition, the theoretical stiffness modeling of the scanner was carried out. According to an effective strain energy method, the stiffness model are obtained, which provides a useful tool to calculate the stiffness of scanner. Furthermore, the characteristics of the XYZ scanner are evaluated in this paper by finite element analysis simulation. The simulation results show that the cross-axis coupling ratio of the proposed scanner is less than 0.91%, indicating excellent decoupling performances. Meanwhile, and the dynamic characteristics are investigated and the results are shown that the design scanner provides the large dynamic bandwidth.**

Keywords—XYZ scanner; Stiffness modeling; Finite element analysis.

I. INTRODUCTION

The atomic force microscope (AFM) plays a significant role in machining, imaging, and manipulating objects at nanometer scale [1, 2]. One of the key components of AFM is a XYZ precision scanner that scans or positions the sample in X-, Y- and Z-directions with high-precision positioning resolution. Scanner will have a significant impact the result of the scanning imaging and operation. It is well know that high-speed operation of an AFM are increasingly required, and it is also a challenge for the researchers. Conventionally, piezoelectric tube scanners are the most widely used scanner in commercial AFMs, because it has excellent resolution, simple structure, easy to install and configure. However, there are two fatal factors limiting the scan efficiency and accuracy of an AFM. These factors include: the low resonance frequency of the piezoelectric tube scanner and the cross coupling error of the piezoelectric tube scanner. Therefore, it should be search another scanner to replace the conventional piezoelectric tube, which have high resonance frequencies and accuracy.

In the past few years, base on flexible hinge structure, several XYZ AFM nanopositioning stages have been reported [3-5], which consists of a XY stage and a Z stage. A number of commercial AFMs has appeared in the market that are equipped with flexure-based nanopositioning platforms[6, 7]. Flexure-guided mechanisms are categorized into two main configurations: serial or parallel. Depending on design requirements, each configuration has been reported. For serial kinematic mechanism, such as, a flexure hinge-based XYZ atomic force microscopy scanner is presented by Kim et al [8]. In this serial-kinematic XY flexure-guided mechanism, measurement uncertainty is dominantly affected by the Abbe error of the XYZ scanning stage. Leang and Fleming [9] presented a two-axis (XY) high-speed serial-kinematic scanning probe microscope (SPM) scanner in 2009. Wadikhaye et al [10] presented a compact XYZ serial-kinematic scanner for high-speed atomic force microscopy in 2011. In 2012, a high-performance XYZ serial-kinematic nanopositioning stage is reported by Kenton and Leang [11], which was integrated with a commercial scan-by-probe atomic force microscope. In addition, for another flexure mechanism: parallel kinematic mechanism, Schitter et al [12] presented a novel scanner for high-speed atomic for microscopy, which enables scanning speeds three orders of magnitude faster than the conventional AFMs. A high-speed atomic force microscopy (HS-AFM) has recently been established by Watanabe et al [13], which was used in video imaging of dynamic processes in live bacterial and eukaryotic cells. Li et al [14] proposed the design, analysis, and testing of a parallel-kinematic high-bandwidth XY nanopositioning stage driven by piezoelectric stack actuators. Klapetek et al [15] presented a large area high-speed measuring system, which enables generating nano-resolution scanning probe microscopy data over mm^2 regions. Yong et al [16] presented a high-speed XYZ nanopositioner based on parallel flexure-guided mechanism. Due to parallel structures offer high motion accuracy and high mechanical stiffness, leading to high resonance frequencies and compactness, parallel flexure-guided mechanism are increasingly utilized in high-speed nanopositioning stages.

This paper presents the design of a parallel kinematic high-speed piezoelectric actuator (PZT) XYZ scanner. The design is aimed at achieving high resonance frequencies and low cross-coupling. The developed stage consists of a parallel kinematic XY stage and a Z stage. The Z stage is mounted on

the central moving platform of the XY stage. To achieve the design objective, several parallel leaf flexure hinge mechanisms, arranging symmetrically around the central moving platform of the XY stage, are utilized to provide large stiffness and reduce cross-coupling. For the Z stage, a symmetrical leaf flexure parallelogram mechanism is adopted to achieve high resonance frequencies and decoupling. The stiffness model of the developed XYZ scanner is established. Then, finite element analysis (FEA) is utilized to validate the characteristics of the XYZ scanner.

The remainder of this paper is organized as follows. Section II starts with introduction mechanical design of the scanner. Section III provides the stiffness analysis of the scanner. In Section IV, finite element analysis (FEA) has been performed to validate the static and dynamic characteristics of the scanner. Conclusions are presented in Section V.

II. Mechanical Desig

The proposed AFM XYZ scanner consists of a XY stage, a Z stage, a base, three piezoelectric actuators (PZTs), two precision capacitive sensors and a sensor target. The assembly and exploded views of the scanner are shown in Fig. 1. The scanner is designed to fit into a Benyuan-CSPM5500 scanning probe microscope.

A. XY Stage

The schematic diagram of the decoupled XY stage is shown in Fig. 2(a). The identical kinematic flexure hinge mechanisms in XY axes guarantee the uniform characteristics of the central moving platform. In the proposed XY stage, the central moving platform (where the Z stage is attached) is connected to four linkages through four parallel flexure mechanisms (five leaf-spring hinges), and four linkages are connected to the frame through another eight parallel flexure mechanisms (three leaf-spring hinges). Due to the symmetric mechanical structure, the stage behavior in the X and Y -axis are the same. The parallel leaf flexure mechanisms is highlighted in dashed lines in Fig. 1 for improve the overall structure of the integration. Benefiting from this design, when the PZT is activated in one direction, the parallel leaf flexure mechanisms transmits the motion to the central moving platform due to its high longitudinal rigidity; while another parallel leaf flexure mechanisms function as a prismatic joint due to their low transverse stiffness in the orthogonal direction, as shown in Fig. 2(a).

B. Z Stage

The Z stage is also designed with a parallel flexure mechanisms, as shown in Fig. 2(b). The end-effector of the Z stage is connected to the fix frame through ten leaf-spring hinges. Ten leaf-spring hinges are located at the same circle with the separation angle of 36°, so that the end-effector of the Z stage can only moves along the Z-axis without cross-axis coupling error. When the Z stage is actuated along the Z-axis, the translational motion of the end-effector is guided by the parallel leaf flexure hinges and no cross-axis error occurs.

In this proposed AFM scanner, the Z stage is mounted on the top of the XY stage. Both two stages were manufactured monolithically using WEDM technology, the material for the scanner is chosen as Aluminum Al7076 T6 with a density of 2700 kg/m^3, a Young's modulus of 70 GPa, a Poisson's ratio of 0.34, and a yield strength of 434 MPa. Compared with other materials, Aluminum 7075-T6 is light weight, strong, and has good fatigue strength.

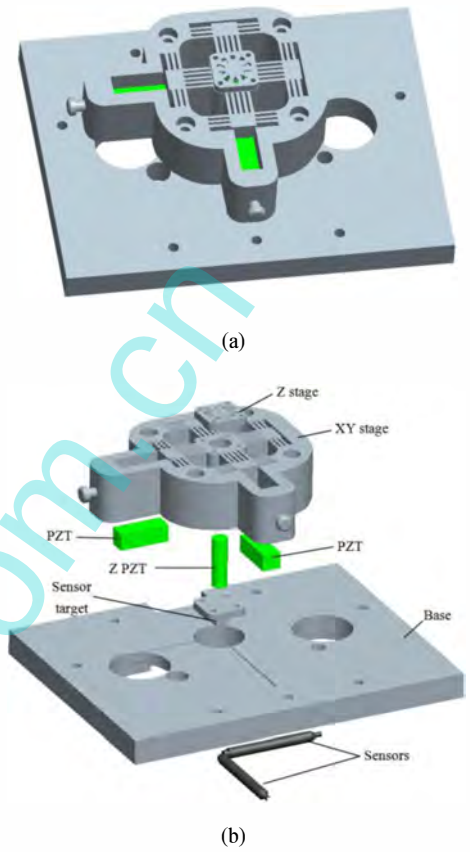

Fig. 1. 3D solid model of the XYZ scanner. (a) Assembly view and (b) Exploded view.

III. Stiffness Modeling

In this section, the strain energy method is used to deduce stiffness matrix of the stage. The overall stiffness matrix $\boldsymbol{K}$ of the stage is the relationship between the applied external load $\boldsymbol{W}$ and the twist $\boldsymbol{\delta}_w$ of the central point of the end-effector. The external load $\boldsymbol{W}$ contains external force $\boldsymbol{F}$ and external moments $\boldsymbol{M}$. The twist $\boldsymbol{\delta}_w$ contains translation $\boldsymbol{\delta}_t$ and rotation $\boldsymbol{\delta}_r$. This relationship can be expressed as

$$\boldsymbol{W} = \boldsymbol{K}\boldsymbol{\delta}_w \tag{1}$$

According to Castigliano's second theorem, the twist of an elastic structure is the partial derivative of the strain energy U of the structure with respect to applied external load, given as

$$\boldsymbol{\delta}_w = \frac{\partial U}{\partial \boldsymbol{W}} \tag{2}$$

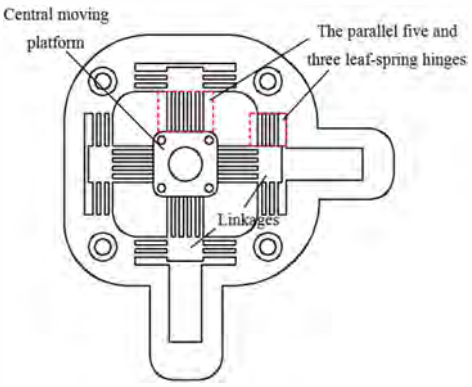

(a)

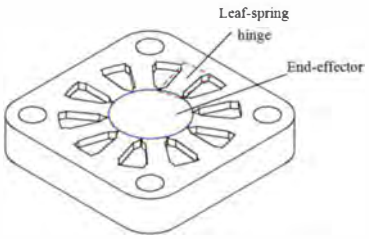

(b)

Fig. 2. (a) Schematic diagram of the XY stage and (b) Schematic diagram of the Z stage

And then, the relationship can be obtained

$$\frac{\partial U}{\partial \boldsymbol{W}} = \boldsymbol{C}\boldsymbol{W} \tag{3}$$

where $\boldsymbol{C}$ is the overall compliance matrix, the stiffness matrix can be obtained as

$$\boldsymbol{K} = \boldsymbol{C}^{-1} \tag{4}$$

To obtain the compliance matrix $\boldsymbol{C}$, the total strain energy of the scanner should be solved. This paper assumes that leaf-spring hinges are flexible, while the other components are infinitely rigid. The strain energy of all leaf-spring hinges are solved respectively and summed to obtain the total strain energy.

Assuming that the end-effector experiences an external load $\boldsymbol{W}$, as shown in Fig. 3, the relation between reaction forces/moments and the applied external load can be written as

$$\begin{cases} \sum_{i=1}^{4} (f_{i1} + f_{i2}) \cdot \boldsymbol{e}_i = \boldsymbol{F} \\ \sum_{i=1}^{4} \left[f_{i1}(\boldsymbol{e}_i \times \boldsymbol{R}) + f_{i2}(\boldsymbol{e}_i \times \boldsymbol{R}) + \boldsymbol{M}_{i1} + \boldsymbol{M}_{i2} \right] = \boldsymbol{M} \end{cases} \tag{5}$$

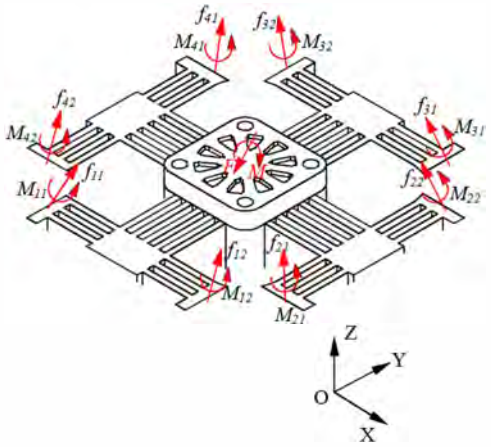

Fig. 3. The applied external load on the end-effector and reaction forces/moments on the XY stage.

In (5), f_{i1}, f_{i2} and $\boldsymbol{M}_{i1}$, $\boldsymbol{M}_{i2}$ denote the reaction forces and the reaction moments exerted at the end of the side of the parallel three leaf-spring hinges, respectively. $\boldsymbol{e}_i$ denotes the unit vector of the reaction force, and $\boldsymbol{R}$ denotes the unit vector of the radius of the end-effector.

Figure 4 shows internal forces and moments experienced by the parallel five (three) leaf-spring hinge. As described in Fig. 4(a), the leaf-spring hinge *F1* experiences three forces f_{F1x}, f_{F1y} and f_{F1z}, and three moments M_{F1x}, M_{F1y} and M_{F1z}. According to the spacial equilibrium force system, the relationship can be obtain:

$$\begin{cases} f_{F1x} = (f_{i1} + f_{i2})\boldsymbol{e}_i \cdot \boldsymbol{l}_i \\ f_{F1y} = (f_{i1} + f_{i2})\boldsymbol{e}_i \cdot \boldsymbol{q}_i \\ f_{F1z} = (f_{i1} + f_{i2})\boldsymbol{e}_i \cdot (\boldsymbol{l}_i \times \boldsymbol{q}_i) \\ M_{F1x} = v(f_{i1} + f_{i2})\boldsymbol{e}_i \cdot (\boldsymbol{l}_i \times \boldsymbol{q}_i) + \boldsymbol{M}_{i1} \cdot \boldsymbol{l}_i + \boldsymbol{M}_{i2} \cdot \boldsymbol{l}_i \\ M_{F1y} = (s_{i1} f_{i1} - s_{i2} f_{i2})\boldsymbol{e}_i \cdot (\boldsymbol{l}_i \times \boldsymbol{q}_i) + \boldsymbol{M}_{i1} \cdot \boldsymbol{q}_i + \boldsymbol{M}_{i2} \cdot \boldsymbol{q}_i \\ M_{F1z} = (s_{i1} f_{i1} - s_{i2} f_{i2})\boldsymbol{e}_i \cdot \boldsymbol{q}_i + v(f_{i1} + f_{i2})\boldsymbol{e}_i \cdot \boldsymbol{l}_i + \\ \qquad \boldsymbol{M}_{i1} \cdot (\boldsymbol{l}_i \times \boldsymbol{q}_i) + \boldsymbol{M}_{i2} \cdot (\boldsymbol{l}_i \times \boldsymbol{q}_i) \end{cases} \tag{6}$$

Similarly, as described in Fig. 4(b), the leaf-spring hinge *T1* experiences forces and moments can be expressed as:

$$\begin{cases} f_{T1x} = f_{i1}\boldsymbol{e}_i \cdot \boldsymbol{l}_i \\ f_{T1y} = f_{i1}\boldsymbol{e}_i \cdot \boldsymbol{q}_i \\ f_{T1z} = f_{i1}\boldsymbol{e}_i \cdot (\boldsymbol{l}_i \times \boldsymbol{q}_i) \\ M_{T1x} = hf_{i1}\boldsymbol{e}_i \cdot (\boldsymbol{l}_i \times \boldsymbol{q}_i) + \boldsymbol{M}_{i1} \cdot \boldsymbol{q}_i \\ M_{T1y} = l_{i1} f_{i1}\boldsymbol{e}_i \cdot (\boldsymbol{l}_i \times \boldsymbol{q}_i) + \boldsymbol{M}_{i1} \cdot \boldsymbol{l}_i \\ M_{T1z} = hf_{i1}\boldsymbol{e}_i \cdot \boldsymbol{l}_i + l_{i1} f_{i1}\boldsymbol{e}_i \cdot \boldsymbol{q}_i + \boldsymbol{M}_{i1} \cdot (\boldsymbol{l}_i \times \boldsymbol{q}_i) \end{cases} \tag{7}$$

where, $\boldsymbol{l}_i$ denotes the unit vector $O'A$, $\boldsymbol{q}_i$ denotes the unit vector $O'O$. v, s_{i1} and s_{i2} denote the length of the vectors $O'O$, $O'A$ and $O'B$, respectively. l denote the length of the leaf-spring

hinge *T1*, *h* denote the width between the leaf-spring hinge *T1* and *T2*.

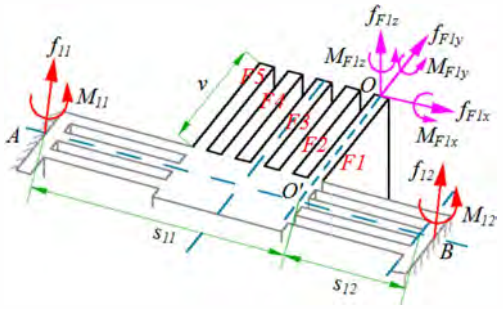

(a)

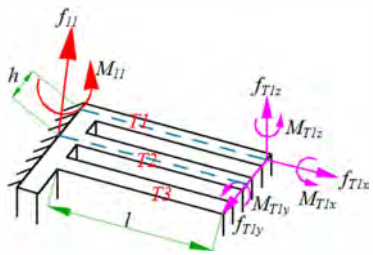

(b)

Fig. 4. The internal forces and moments experienced by (a) the parallel five leaf-spring hinge and (b) the parallel three leaf-spring hinge.

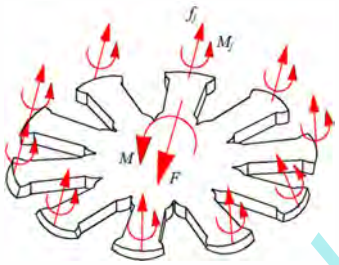

(a)

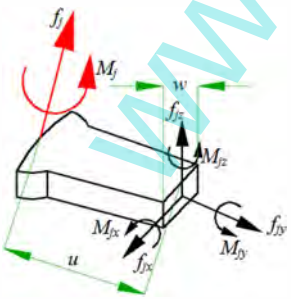

(b)

Fig. 5. (a) The applied external load and reaction forces/moments on the end-effector, (b) The internal forces and moments experienced by leaf hinge.

As shown in Fig. 5(a), the relation between reaction forces/moments of Z stage and the applied external load can be written as

$$\begin{cases} \sum_{j=1}^{10} f_j \cdot \boldsymbol{g}_j = \boldsymbol{F} \\ \sum_{j=1}^{10} [f_j (\boldsymbol{g}_j \times \boldsymbol{r}) + \boldsymbol{M}_j] = \boldsymbol{M} \end{cases} \tag{8}$$

As described in Fig. 5(b), the flexible hinge of Z stage experiences forces and moments can be expressed as:

$$\begin{cases} f_{jx} = f_j \cdot \boldsymbol{g}_j \cdot \boldsymbol{w} \\ f_{jy} = f_j \cdot \boldsymbol{g}_j \cdot \boldsymbol{u} \\ f_{jz} = f_j \cdot \boldsymbol{g}_j \cdot (\boldsymbol{w} \times \boldsymbol{u}) \\ M_{jx} = \boldsymbol{u} \cdot f_j \cdot \boldsymbol{g}_j \cdot (\boldsymbol{w} \times \boldsymbol{u}) + \boldsymbol{M}_j \cdot \boldsymbol{w} \\ M_{jy} = 0 \\ M_{jz} = \boldsymbol{u} \cdot f_j \cdot \boldsymbol{g}_j \cdot \boldsymbol{w} + \boldsymbol{M}_j \cdot (\boldsymbol{w} \times \boldsymbol{u}) \end{cases} \tag{9}$$

where, f_j and $\boldsymbol{M}_j$ denote the reaction forces and the reaction moments exerted at the flexible hinge of Z stage, respectively. $\boldsymbol{g}_i$ denotes the unit vector of the reaction force, and $\boldsymbol{r}$ denotes the unit vector of the radius of the end-effector. $\boldsymbol{w}$ denotes the unit vector w, $\boldsymbol{u}$ denotes the unit vector u. w and u denote the length and width of the flexible hinge, respectively.

With the internal forces and moments, the strain energy of the leaf-spring hinge *F1* and *T1* on the parallel five and three leaf-spring hinge can be obtained, respectively. The strain energy of the flexible hinge of Z stage also can be obtained.

$$\begin{cases} U_{F1} = \int_{OO'} \left(\frac{M_{F1x}^2}{2EI_{xx}} + \frac{M_{F1y}^2}{2GJEI_{yy}} + \frac{M_{F1z}^2}{2EI_{zz}} + \frac{f_{F1x}^2}{2GA_x} + \frac{f_{F1y}^2}{2EA_y} + \frac{f_{F1z}^2}{2GA_z} \right) dv \\ U_{T1} = \int_{l} \left(\frac{M_{T1x}^2}{2EI_{xx}} + \frac{M_{T1y}^2}{2GJEI_{yy}} + \frac{M_{T1z}^2}{2EI_{zz}} + \frac{f_{T1x}^2}{2GA_x} + \frac{f_{T1y}^2}{2EA_y} + \frac{f_{T1z}^2}{2GA_z} \right) dl \\ U_j = \int_{u} \left(\frac{M_{jx}^2}{2EI_{xx}} + \frac{M_{jy}^2}{2GJEI_{yy}} + \frac{M_{jz}^2}{2EI_{zz}} + \frac{f_{jx}^2}{2GA_x} + \frac{f_{jy}^2}{2EA_y} + \frac{f_{jz}^2}{2GA_z} \right) du \end{cases} \tag{10}$$

where E and G denote the elastic modulus and the shear modulus of the stage; I_{xx}, I_{yy} and I_{zz} denote the area moment of inertia of the hinge cross section about the X, Y and Z axes; J denotes the polar moment of inertia of the hinge cross section; A_x, A_y and A_z denote the effective area of the hinge cross section along the X, Y and Z axes.

Similarly, the strain energy of the leaf-spring hinge *F2*, *F3*, *F4*, *F5* and *T2*, *T3* can be calculated, respectively. Therefore, the total strain energy of the XYZ scanner is given by

$$U_{Total} = U_{F1} + U_{F2} + U_{F3} + U_{F4} + U_{F5} + U_{T1} + U_{T2} + U_{T3} + 10 \cdot U_j \quad (11)$$

And then, according to the above (3) and (4), the stiffness matrix of the XYZ scanner can be obtained.

IV. Characteristic Analysis

Finite element analysis (FEA) is conducted to validate the established models and obtain further insights into the static and dynamic characteristics of the developed XYZ scanner. The commercial finite element software ANSYS is utilized to perform the analyses. The material for the scanner is chosen as Aluminum 7075-T6 with a density of 2770 kg/m^3, a Young's modulus of 71 GPa, and a Poisson's ratio of 0.33. Both of the XY and Z stages are bonded together. In order to improve the computational accuracy, the mapping mesh method is adopted. The mesh is strictly controlled in the areas of flexure hinges, where the large deformation is generally occurred.

A. Static Characteristic

In order to investigate the motion characteristics of the system, the static characteristic analysis is carried out. The in-plane stiffness of the scanner should be high so as to increase the rejection capability against external disturbances. The different working style of the driven PZTs and the analysis results are shown in Fig. 6, the corresponding output displacement of the scanner are obtained. It shows that the linear stiffness without and with PEAs installed are 45.63, 45.65 and 4.63 N/μm in the X, Y and Z direction, respectively. However, the out-of-plane stiffness of the XY stage is a key factor in determining its capacity of resisting disturbance. The simulation analyses show that an out-of-plane stiffness of 208.3 N/μm is achieved. As a result, the out-of-plane stiffness of the central moving platform is more stiff than the Z stage.

The cross-coupling effect among the three axes has been one of the complications that affects the accuracy of AFM. Fig. 6 shows the cross-coupling motions of the scanner. When a driving force was applied to the X axis, the induced Y and Z displacements were 0.41% and 0.82% of the X displacement respectively. Due to the structure symmetry, similar result in the Y axis is obtained. When the Z axis is being driven, it induces 0.89% in the X displacement and 0.91% in the Y displacement. The results demonstrate the excellent decoupling capability of the scanner.

B. Dynamic Characteristic

In order to further examine performance of the scanner described above, the dynamic characteristics of the scanner are investigated and the results are shown in Fig. 7. If no PZTs are installed in the scanner, the first two mode shape are moved along the X-axis and Y-axis with the frequency of 7320.6 Hz and 7321.1 Hz, respectively; Both the third and fourth modes shape are moved along the Z-axis, with the corresponding frequencies of 18512 Hz and 20815 Hz, respectively. However, the third mode, only the end-effector of Z stage is moved along the Z-axis, and the fourth mode, both the central moving platform of the XY stage and the end-effector of Z stage are moved along the Z-axis. If the PZTs are installed, it can be realized by incorporating spring-damper components into the scanner. It is considered as a spring with a constant stiffness *k*, one end of the spring is fixed and the other end is attached on the movable end, as shown in Fig. 8. The simulation results show that the first fourth natural frequencies increase to 9286.04 Hz, 9287.13 Hz, 21013 Hz and 23162 Hz, respectively, and the similar corresponding mode shapes are obtained.

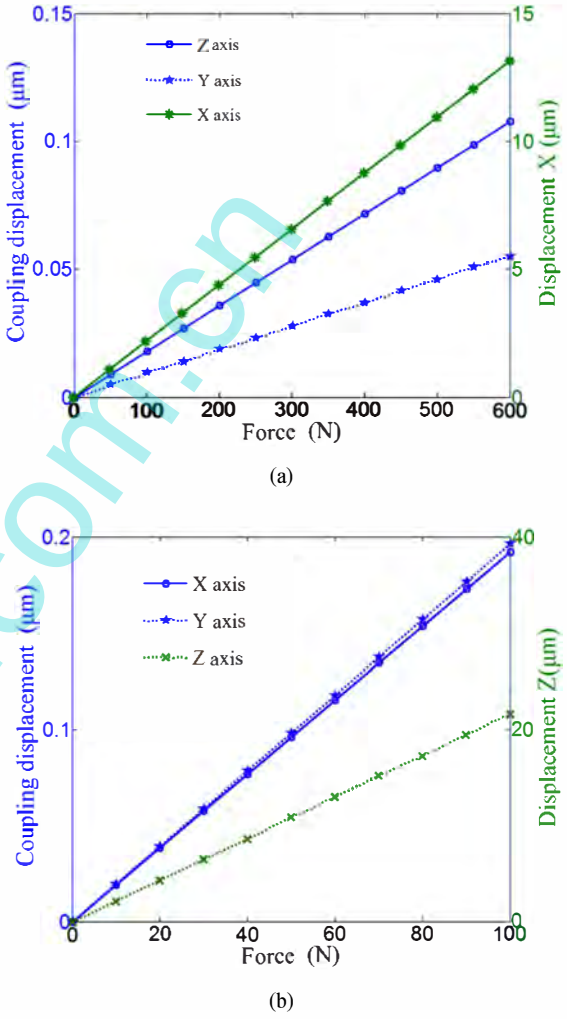

Fig. 6. (a) Cross-axis coulping when X axis is activated and (b) Cross-axis coulping when Z axis is activated.

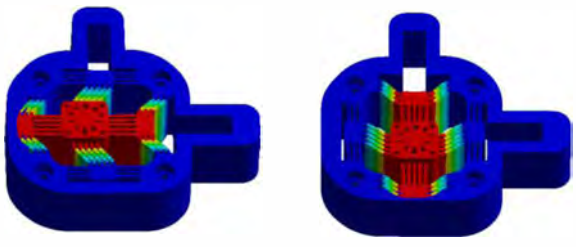

(a) (b)

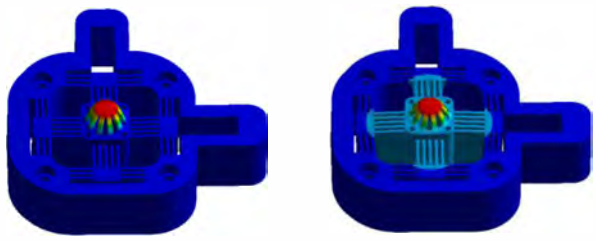

(c) (d)

Fig. 7. First fourth mode shapes of the scanner with no PZTs installed: (a) first mode shape (7320.6 Hz), (b) second mode shape (7321.1 Hz), third mode shape (18512 Hz) and fourth mode shape (20815 Hz).

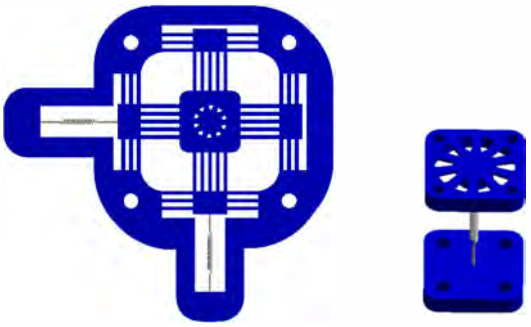

(a) (b)

Fig. 8. Spring components are installed in scanner, (a) XY stage and (b) Z stage.

V. Conclusion

This paper presents the design of a parallel kinematic high-speed piezoelectric actuator (PZT) XYZ scanning stage. The presented stage consists of a parallel kinematic XY stage and a Z stage. Both manufactured using the wire electrical discharge machining (WEDM) technology. The Z stage is mounted on the central moving platform of the XY stage. In addition, the stiffness modeling of this scanner system is investigated. According to an effective strain energy method, the stiffness model are obtained. Then, finite-element analysis (FEA) is utilized to validate the proposed scanner. The static and dynamic characteristics of the scanner have been investigated. The simulation results show that the cross-axis coupling ratio of the proposed scanner is below 0.91%, indicating excellent decoupling performances. Meanwhile, the dynamic characteristic demonstrates that the design structure provides the high dynamic bandwidth with the lowest resonant frequency of 7320.6 Hz, which ensures that the system has good dynamic characteristic.

Acknowledgment

This research is supported by National Natural Science Foundation of China (Nos. 51275337, 51205279, 51420105007, 51505330).

References

[1] T. Ando. High-speed AFM imaging. Current Opinion in Structural Biology 2014; 28: 63-68.

[2] S. S. Park, M. G. Mostofa, C. I. Park, M. Mehrpouya, S. Kim. Vibration assisted nano mechanical machining using AFM probe. CIRP Annals-Manufacturing Technology 2014; 63 (1): 537-540.

[3] Asylum research, see http://asylumresearch.com for information on flexure-based nanopositioning platforms.

[4] Park Systems, see www.parkafm.com for information on the use of flexure-based nanopositioning platforms in commercially available AFMs.

[5] T. Ando, N. Kodera, D. Maruyama, E. Takai, K. Saito, and A. Toda, "A high-Speed atomic force microscope for studying biological macromolecules in action," Jpn. J. Appl. Phys., vol. 41, no. 7B, pp. 4851-4856, 2002.

[6] G. Schitter, K. J. Astrom, B. DeMartini, P. J. Thurner, K. L. Turner, and P. K. Hansma, "Design and modeling of a high-speed AFM-scanner," IEEE Trans. Contr. Syst. Tech., vol. 15, no. 5, pp. 906-915, 2007.

[7] Y. K. Yong and S. O. R. Moheimani, "Design, modeling, and FPAA-based control of a high-speed atomic force microscope nanopositioner," IEEE/ASME Trans. Mechatron., vol. 18, no. 3, pp. 1060-1071, 2013.

[8] D. Kim, D. Kang, J. Shim, I. Song, D. Gweon, "Optimal design of a flexure hinge-based XYZ atomic force microscopy scanner for minimizing Abbe errors," Rev. Sci. Instrum., vol. 76, no. 7, pp. 1-6, 2005.

[9] K. K. Leang and A. J. Fleming, "High-speed serial-kinematic SPM scanner: Design and drive consideration," Asian J. Control, Vol. 11, No. 2, pp. 144-153, March 2009.

[10] S.P. Wadikhaye, Y.K. Yong, S.O.R. Moheimani, "Design of a compact serial-kinematic scanner for high-speed atomic force microscopy: an analytical approach," Micro Nano Lett., vol. 7, no. 4, pp. 309-313, 2012.

[11] B. Kenton and K. Leang, "Design and control of a three-axis serial-kinematic high-bandwidth nanopositioner," IEEE/ASME Trans. Mechatron., vol. 17, no. 2, pp. 356-369, 2012.

[12] G. Schitter, P. J. Thurner, P. K. Hansma, "Design and input-shaping control of a novel scanner for high-speed atomic force microscopy," Mechatronics, Vol. 18, no. 5-6, pp. 282-288, June 2008.

[13] H. Watanabe, T. Uchihashi, T. Kobashi,M. Shibata, J. Nishiyama, R. Yasuda and T. Ando, "Wide-area scanner for high-speed atomic force microscopy," Rev. Sci. Instrum., vol. 84, no. 5, pp. 1-10, 2013.

[14] C. X. Li, G. Y. Gu, M. J. Yang and L. M. Zhu, "Design, analysis and testing of a parallel-kinematic high-bandwidth XY nanopositioning stage," Rev. Sci. Instrum., vol. 84, no. 12, pp. 1-12, 2013.

[15] P. Klapetek, M. Valtr, L. Picco, O. D. Payton, J. Martinek, A. Yacoot and M. Miles, "Large area high-speed metrology SPM system," Nanotechnology, vol. 26, no. 6, pp. 1-9, 2015.

[16] Y. K. Yong, S. O. R. Moheimani, "Collocated Z-Axis Control of a High-Speed Nanopositioner for Video-Rate Atomic Force Microscopy," IEEE Trans. Nanotechnol., vol. 14, no. 2, pp. 338-345, March 2015.